Shift of tellurium solid-solubility limit and enhanced thermoelectric performance of bismuth antimony telluride milled with yttria-stabilized zirconia balls and vessels

Jun Asai[a], Mongkol Bumrungpon[b], Toshiya Tsubochi[a], Takayuki Kanaya[a], Masaya Tachii[a], Toshiki Maeda[a] and Kazuhiro Hasezaki[c]

[a]*Department of Mechanical Science, Division of Science and Technology, Graduate School of Sciences and Technology for Innovation, Tokushima University, 2-1 Minamijyousanjima, Tokushima 770-8506, Japan*

[b]*Graduate School of Advanced Technology and Sciences, Tokushima University, 2-1 Minamijyousanjima, Tokushima 770-8506, Japan*

[c]*Department of Mechanical Science, Graduate School of Technology, Industrial and Social Sciences, Tokushima University, 2-1 Minamijyousanjima, Tokushima 770-8506, Japan*

**Corresponding author: hasezaki@tokushima-u.ac.jp*

As a thermoelectric material, $Bi_{0.3}Sb_{1.7}Te_{3.0+x}$ (x = 0–0.05) was fabricated by mechanical alloying using yttria-stabilized zirconia (YSZ) ceramic balls and vessels, followed by hot pressing. The effects of the added tellurium on the thermoelectric properties of $Bi_{0.3}Sb_{1.7}Te_{3.0}$ fabricated with YSZ milling media were investigated. All sintered samples were isotropic and showed *p*-type conduction. The tellurium solid-solubility limit for $Bi_{0.3}Sb_{1.7}Te_{3.0}$ was determined to be x = 0.01 by differential thermal analysis (DTA). The solid-solubility limit of the sample fabricated using YSZ was narrower than that of the congener prepared with Si_3N_4 balls and stainless-steel metal vessels. Among the evaluated compositions, the $Bi_{0.3}Sb_{1.7}Te_{3.01}$ sintered disk had the highest dimensionless figure of merit, ZT = 1.30, at room temperature. This value was superior to that of $Bi_{0.3}Sb_{1.7}Te_{3.0+x}$ fabricated using metal vessels. Thus, selection of the milling media affected the optimum doping amount and maximum ZT.

Keywords: hot pressing; milling; electrical properties; thermal conductivity; zirconia

1. Introduction

Thermoelectric materials and systems enable the direct conversion of heat into electricity and vice versa by the Seebeck and Peltier effects. Thermoelectric materials have great potential for application in waste-heat recovery and solid-state refrigeration of small areas because of their many advantages, such as the lack of moving parts, lightness, environmental friendliness, and high reliability [1–3]. However, thermoelectric materials are not widely used owing to their low energy conversion efficiency. In recent years, methods of improving the thermoelectric performance of materials such as ~~metal~~ chalcogenides [4–9], skutterudites [10–12], and silicides [13,14] have been studied.

The performance of thermoelectric materials is estimated by the dimensionless figure of merit, ZT:

$$ZT = \alpha^2 \sigma \kappa^{-1} T \qquad (1)$$

where α is the Seebeck coefficient (V K^{-1}), σ is the electrical conductivity (S m^{-1}), κ is the thermal conductivity (W m^{-1} K^{-1}), and T is the absolute temperature (K). The thermal conductivity κ is generally expressed by the following simple formula:

$$\kappa = \kappa_{\text{phonon}} + \kappa_{\text{carrier}} = \kappa_{\text{phonon}} + L\sigma T \qquad (2)$$

The carrier thermal conductivity, κ_{carrier}, is given by the Wiedemann-Franz law, where κ_{phonon} is the phonon thermal conductivity, and L is the Lorenz number [15,16].

Bi_2Te_3-based materials are regarded as having the best thermoelectric properties near room temperature. These materials adopt a rhombohedral crystal structure, with space group $R3m$. They have remarkable anisotropic thermoelectric and physical properties [17]. The powders-solid state milling reaction (sometimes called mechanical alloying (MA)) followed by hot pressing (HP) is a widely investigated method of preparing these materials [18–20]. MA is a high-energy powder processing method that provides fine-

grained powders and uniform elemental dispersion. The sintered samples obtained via the MA-HP process show low phonon thermal conductivity, and HP exerts refining effect via grain boundary scattering [21]. The resulting compacts fabricated by the MA-HP process have random crystal orientations and refined structures, which strongly contribute to reducing the phonon thermal conductivity.

A previous study [22] showed that the $Bi_{0.3}Sb_{1.7}Te_{3.0}$ composition was optimal for undoped *p*-type Bi_2Te_3-Sb_2Te_3 materials prepared by MA-HP. This composition is different from that prepared by melt growth, namely $Bi_{0.5}Sb_{1.5}Te_{3.0}$ [23]. It was also confirmed that single-phase and isotropically oriented Bi_2Te_3-Sb_2Te_3 could be obtained by the MA-HP process [22]. In recent years, the effect of milling media composed of balls and vessels on $Bi_{0.3}Sb_{1.7}Te_{3.0}$ has been investigated. The disks fabricated by milling with yttria-stabilized zirconia (YSZ) ceramic balls and vessels showed better thermoelectric performance than the disks fabricated by using Si_3N_4 balls and stainless-steel vessels because the YSZ milling media suppressed contamination from the milling media, where the contaminants act as a carrier dopant [24].

Various strategies have been investigated to improve the *ZT,* such as dopant addition [25–29], nanoparticle dispersion [30–34], and adjusting the fabrication process [35–37]. Dopant addition is a notably effective way to control thermoelectric properties. Deviation from stoichiometry due to constituent elemental doping has impacts on the structural properties, transport properties and the type of defects inside materials [38–40]. In *p*-type $Bi_{0.3}Sb_{1.7}Te_{3.0}$, non-stoichiometry by tellurium doping improved *ZT*. A previous study showed that the *ZT* of $Bi_{0.3}Sb_{1.7}Te_{3.0+x}$ reached a maximum value of 1.11 with a tellurium content of $x = 0.1$, and excess Te acted as a carrier dopant, thereby improving *ZT* [27]. However, Si_3N_4 balls and stainless-steel vessels were used in that study, and

contamination from the milling media affected the thermoelectric properties and optimum tellurium composition. If the milling media material is appropriate, it is expected that the variations in the thermoelectric properties due to dopant addition could be adjusted and the optimum dopant amount would differ.

The effect of adding tellurium on the thermoelectric properties of $Bi_{0.3}Sb_{1.7}Te_{3.0}$ fabricated with YSZ milling media has not been reported previously. In this study, tellurium-doped *p*-type $Bi_{0.3}Sb_{1.7}Te_{3.0}$ is fabricated by the MA-HP process using YSZ milling media. The effect of tellurium as an additive on the thermoelectric properties of isotropic $Bi_{0.3}Sb_{1.7}Te_{3.0}$ fabricated with YSZ milling media is investigated.

2. Materials and methods

High-purity Bi (5N), Sb (6N), and Te (6N) were purchased from Kojundo Chemical Laboratory Co., Ltd., Saitama, Japan, and weighed according to the stoichiometric ratio of $Bi_{0.3}Sb_{1.7}Te_{3.0+x}$ (x = 0, 0.006, 0.01, 0.015, 0.02, 0.035, and 0.05). Only millimeter-scale grains were used as raw materials in order to suppress contamination from the surface oxide layers. The raw materials were loaded into the YSZ vessels with YSZ milling balls with a diameter of 25 mm. The YSZ milling vessels and balls were used to suppress the introduction of contaminants from the milling media, where the contaminants act as carrier dopants and deteriorate the thermoelectric properties. The weight ratio of the milling balls to the starting grains was 20:1. The vessel was sealed in a glove box under Ar atmosphere. MA was performed in a Fritsch P-5 planetary ball-mill at a rotational speed of 150 rpm for 30 h. The resulting powder was passed through a 150 μm diameter sieve, and it was confirmed that no elemental grains remained on the sieve. The as-milled powders were subsequently loaded into an HP mold and placed in an HP chamber. The HP chamber was evacuated to below 0.4 Pa and then filled with Ar gas. The milled powder was hot-pressed at 623 K under a uniaxial pressure of 147 MPa. The sintered sample was a cylinder with a height of 9 mm and diameter of 10 mm. The sample was cut into disks with a thickness of 1.0 mm and a diameter of 10 mm. The disks obtained from both ends of the cylinder were not used in the measurements because they promote the formation of the (0 0 l) texture by plastic deformation and exhibit anisotropic thermoelectric properties [41].

The phases of the sintered disks with x = 0, 0.01, and 0.05 were characterized by X-ray diffraction using Cu-Kα radiation in the Bragg angle range of 2θ = 10–110° with a step size of 0.1° and a step speed of 5.0 s per step (Rigaku SmartLab). In addition, by taking

the disk with $x = 0.01$ for an example, the XRD patterns of the disk sections parallel (in-plane) and perpendicular (out-of-plane) to the pressing direction were investigated. The orientation factor F was estimated by using the Lotgering method to evaluate the isotropy [34]. F is expressed by the following equations:

$$F = (P - P_0) / (1 - P_0) \quad (3)$$

$$P = \Sigma I(00l) / \Sigma I(hkl) \quad (4)$$

$$P_0 = \Sigma I_0(00l) / \Sigma I_0(hkl) \quad (5)$$

where P is the ratio of the intensity summation of the diffraction peaks standing for ($00l$) planes to the counterpart for the (hkl) planes. P_0 is the ratio for the composites with random orientation. $F = 0$ for a random orientation and $F = 1$ for a complete ($00l$) orientation [22]. $P_0 = 0.0486$ was calculated by using standard peaks of $Bi_{0.3}Sb_{1.7}Te_{3.0}$ (Inorganic Crystal Structure Database (ICSD) #184248) [42].

Disks with $x = 0$, 0.01, and 0.05 were ground with a pestle and subjected to differential thermal analysis (DTA; Hitachi TG/DTA6300) to confirm the existence of elemental Te. DTA was performed in the temperature range of 300–1000 K at a constant heating rate of 10 K min^{-1} under Ar gas flow.

The microstructures in the out-of-plane directions and the in-plane fracture surfaces of the disk with $x = 0.01$ were investigated using a scanning electron microscope (SEM; JEOL, JSM-6510A). The elemental distribution profiles of the disk with $x = 0.05$ were analyzed by energy-dispersive X-ray spectroscopy (EDS).

The electrical conductivity, Seebeck coefficient, and thermal conductivity of all the sintered disks were measured at room temperature, and the dimensionless figure of merit, ZT, at room temperature was estimated using Eq. (1). The electrical conductivity was measured by a four-point probe (tungsten carbide, 1.00 mm diameter) test using a delta-

mode electrical resistance system (2182A/6220 instrument; Keithley Instruments, Inc.). Ohmic contact was used to confirm that all measurements had an accuracy better than ±1% [43]. The Seebeck coefficients were measured using the thermal contact method [44]. SRM3451 was used to confirm that the measurement system accuracy was within ±2% [45]. The thermal conductivities were determined using a static comparison method under 1 Pa vacuum [23,46,47]. The standard material for this system was a quartz (κ = 1.411 W m^{-1} K^{-1}) disk with a thickness of 1.0 mm and a diameter of 10 mm. The accuracy of the thermal conductivity measurement system was within ±1%. The phonon and carrier thermal conductivities were estimated using Eq. (2), where the Lorenz number (L) was estimated from the Seebeck coefficient using the effective mass model [48].

The temperature-dependence of the electrical conductivity and Seebeck coefficient for the compacts with x = 0 and 0.01 was examined using a ZEM-3 (Advance-Riko) instrument in the temperature range of 300–580 K. To eliminate the influence of anisotropy, rectangular samples with dimensions of 3.0 × 3.0 × 8.5 mm^3 were cut from the center of the sintered bulks by using a diamond saw blade. The accuracy of the Seebeck coefficient and electrical conductivity from the ZEM-3 measurements was less than ±7%. The relationship between the figure of merit, ZT, and temperature was determined from the temperature-dependence of the electrical conductivity and Seebeck coefficient measured using ZEM-3, and the fixed thermal conductivity at room temperature.

3. Results and Discussion

All the resulting samples were dense and showed *p*-type conduction. Figure 1(a) shows the XRD patterns of the sintered disks with $x = 0$, 0.01, and 0.05. All the main diffraction peaks were consistent with the standard peaks of $Bi_{0.3}Sb_{1.7}Te_{3.0}$ (Inorganic Crystal Structure Database (ICSD) #184248), indicating that the bulk comprised single-phase Bi_2Te_3-Sb_2Te_3 solid-solutions [42]. No additional diffraction peaks associated with pure tellurium were detected. The *F* values for each sample were estimated by using Eq. (3) – (5), to be 0.044, 0.046, and 0.039 respectively, which means that no preferential orientation formed in the obtained sample [34]. Figure 1(b) shows the XRD patterns of the $Bi_{0.3}Sb_{1.7}Te_{3.01}$ sintered disk sections parallel and perpendicular to the pressing direction. The *F* values for the sections parallel and perpendicular to the pressing direction were 0.060 and 0.046 respectively. The result suggests that the disk is regarded as isotropic.

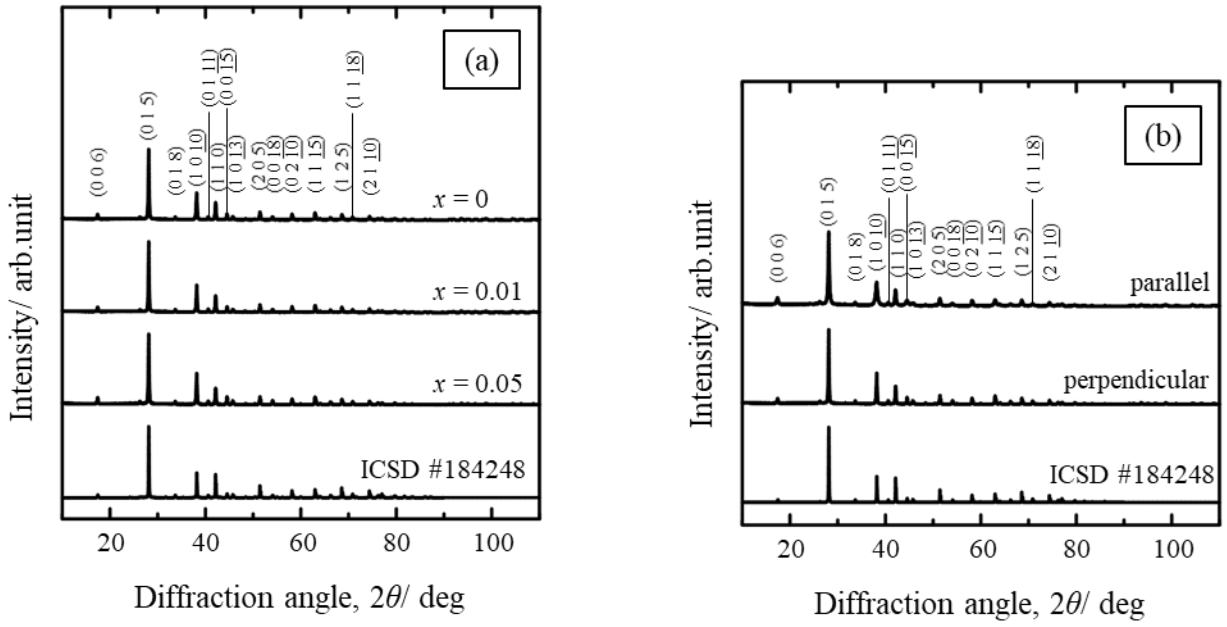

Fig. 1 (a) XRD patterns (2θ = 10–110°) of $Bi_{0.3}Sb_{1.7}Te_{3.0+x}$ sintered disks section perpendicular to the pressing direction prepared by MA-HP, (b) XRD patterns (2θ = 10–

110°) of the $Bi_{0.3}Sb_{1.7}Te_{3.01}$ sintered disk sections parallel and perpendicular to the pressing direction, and Bi_2Te_3-Sb_2Te_3 main indexes [42]. The standard peaks correspond to $Bi_{0.3}Sb_{1.7}Te_{3.0}$ (ICSD #184248).

Figure 2(a) shows the DTA data in the range of 300–1000 K for the samples with x = 0, 0.01, and 0.05. An endothermic peak at approximately 873 K was observed for each sample, which corresponds to the melting point of $Bi_{0.3}Sb_{1.7}Te_{3.0}$. Figure 2(b) shows the magnified DTA curves in the temperature range of 640–720 K. Only the sample with x = 0.05 showed an endothermic peak at approximately 680 K, corresponding to the eutectic point of Te and Bi_2Te_3 [23,49]. This observation indicates that $Bi_{0.3}Sb_{1.7}Te_{3.0+x}$ bulk with $x \leq 0.01$ comprised a single-phase Bi_2Te_3-Sb_2Te_3 solid-solution because the excess Te was dissolved in the $Bi_{0.3}Sb_{1.7}Te_{3.0}$ matrix. On the other hand, excess Te precipitated and formed a Bi_2Te_3-Te solid-solution in the range of $x > 0.01$. Further, the tellurium solid-solubility limit of the $Bi_{0.3}Sb_{1.7}Te_{3.0}$ bulk fabricated by using the YSZ milling vessels and balls was determined as approximately x = 0.01. This is completely different from that of the $Bi_{0.3}Sb_{1.7}Te_{3.0}$ bulk fabricated by using Si_3N_4 milling balls and stainless-steel vessels (x = 0.1) [27].

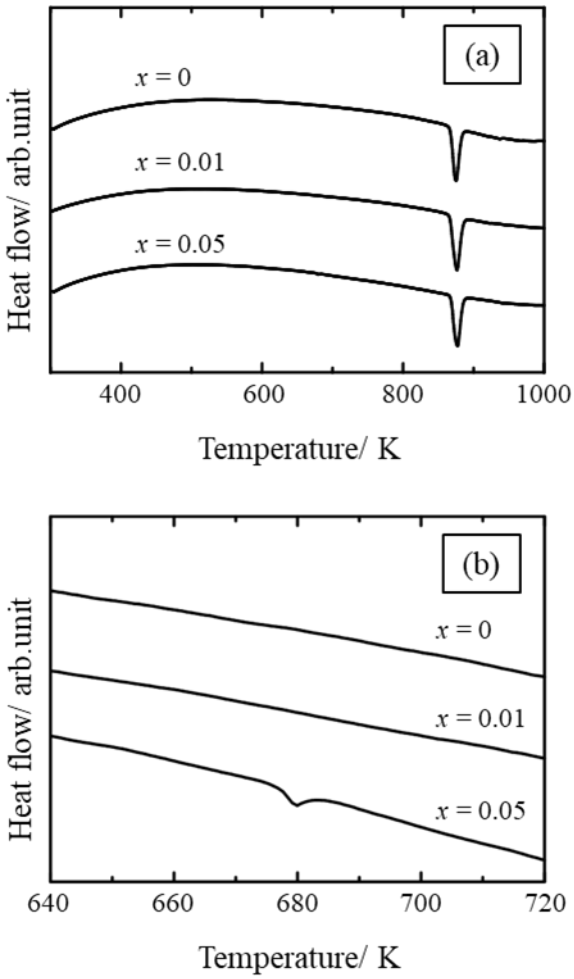

Fig. 2 DTA curves for pestle-ground, sintered samples of $Bi_{0.3}Sb_{1.7}Te_{3.0+x}$ prepared by MA-HP. (a) 300–1000 K, (b) 640–720 K.

Figure 3(a) shows a SEM micrograph of the cross-section of the sintered $Bi_{0.3}Sb_{1.7}Te_{3.01}$ bulk. The bulk was dense and homogeneous throughout the sample. Figure 3(b) shows a SEM micrograph of the fracture surface of the sintered $Bi_{0.3}Sb_{1.7}Te_{3.01}$ bulk. The grain size was approximately 1 μm at the in-plane fracture surface, similar to that of the $Bi_{0.3}Sb_{1.7}Te_{3.0}$ disk [24]. These results show that the amount of Te additive did not affect the grain growth of the matrix. In the sintered $Bi_{0.3}Sb_{1.7}Te_{3.05}$ disk, no apparent precipitated tellurium was confirmed by EDS (Supplementary figure 1). It might be

because the additive tellurium content was less than 1 at %, and it was too small to observe the precipitation by EDS. No reaction between bismuth antimony telluride matrix and contaminants from YSZ milling media was confirmed by EDS in a previous study [24].

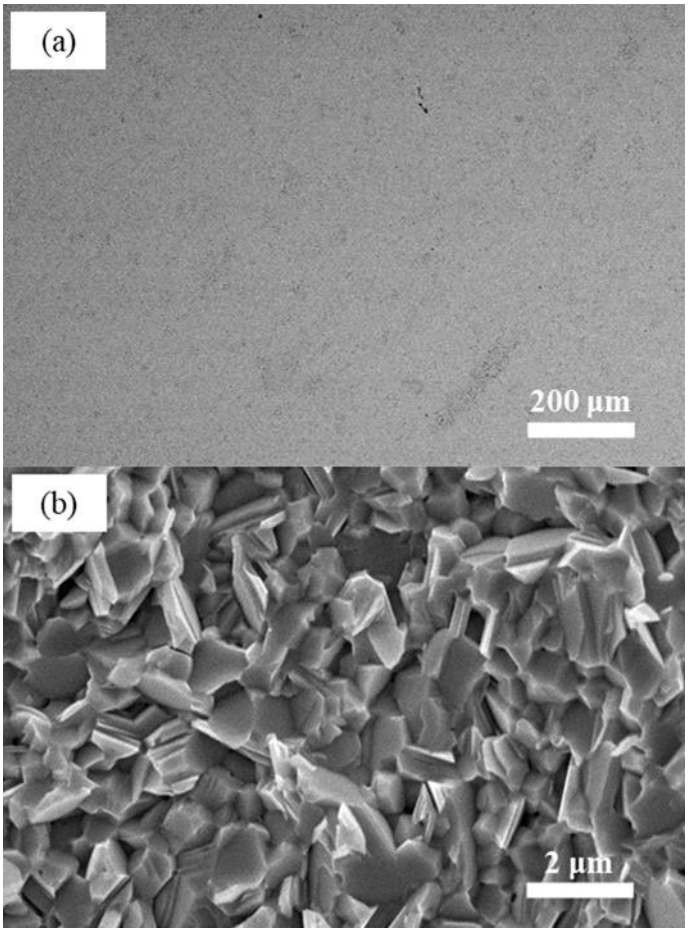

Fig. 3 SEM micrographs of (a) cross-section and (b) fracture surface of $Bi_{0.3}Sb_{1.7}Te_{3.01}$ sintered sample.

Figure 4(a) shows the measured Seebeck coefficients for all sintered disks at room temperature. All Seebeck coefficients were positive, indicating *p*-type semiconductors. The Seebeck coefficient decreased with increasing addition of tellurium, x, and reached the lowest value at $x = 0.01$. In contrast, the Seebeck coefficients were constant in the range of $x > 0.01$. Figure 4(b) shows the measured electrical conductivities of all sintered

disks at room temperature. The electrical conductivity followed a trend opposite to that of the Seebeck coefficient. The electrical conductivity increased with increasing tellurium content, x, and reached a maximum value at $x = 0.01$. For $x \geq 0.01$, the electrical conductivity became constant. These results and the DTA data presented in Fig. 2(b) indicate that the additional tellurium was dissolved in the matrix and acted as a carrier dopant in the range of $x \leq 0.01$. Within this range, additive tellurium formed acceptor levels in the Bi_2Te_3-Sb_2Te_3 system, which caused the variation of band structure and thermoelectric properties [23]. On the other hand, at $x > 0.01$, Te was precipitated and a Bi_2Te_3-Te solid-solution was formed, neither of which affected the thermoelectric properties of $Bi_{0.3}Sb_{1.7}Te_{3.0}$. Additive tellurium was not dissolved in the matrix within this range, which means no variation of acceptor levels and band structures in the Bi_2Te_3-Sb_2Te_3 system. Furthermore, additive tellurium content is quite low as shown in XRD and SEM-EDS results. Due to the above reasons, the thermoelectric properties became constant at $x > 0.01$. This trend was the same as that observed for the bulk fabricated using Si_3N_4 milling balls and stainless-steel vessels. However, the tellurium solid solubility limit for the $Bi_{0.3}Sb_{1.7}Te_{3.0}$ matrix was completely different. The tellurium solid-solubility limit for the $Bi_{0.3}Sb_{1.7}Te_{3.0}$ bulk shifted from $x = 0.1$ to $x = 0.01$ upon changing the milling media from Si_3N_4 balls and stainless-steel vessels to YSZ milling balls and vessels [27]. The shift in the solid solubility limit might be because the contaminants from the YSZ milling media did not react with tellurium. Furthermore, contaminants from the YSZ milling media did not act as carrier dopants. In the case of the Si_3N_4 balls and stainless-steel vessels, the contaminants (such as iron) reacted with tellurium (Supplementary figure 2), and the reactant affected the Seebeck coefficient and electrical conductivity [27]. On the other hand, in the case of YSZ milling media, the ZrO_2 contaminant suppressed

the reaction and did not affect the dopant [24]. The selection of the milling media affected the optimum doping.

Figure 4(c) presents the total, phonon, and carrier thermal conductivities of the sintered $Bi_{0.3}Sb_{1.7}Te_{3.0+x}$ bulk samples at room temperature. The phonon and carrier thermal conductivities were calculated using Equation (2): L was calculated from the Seebeck coefficient by using an effective mass model and was estimated to be approximately 1.6 $\times 10^{-8}$ W Ω K^{-2} for each sample [48]. The phonon thermal conductivity was almost constant for all samples. This suggests that the amount of tellurium added and tellurium precipitation did not contribute to the phonon thermal conductivity due to the quite small content of additive tellurium as with the Seebeck coefficient and electrical conductivity.

Figure 4(d) presents the dimensionless figure of merit, ZT, at room temperature (T = 300 K) for all sintered disks. The ZT value increased upon doping with tellurium, and the $Bi_{0.3}Sb_{1.7}Te_{3.01}$ sample had the highest ZT value of 1.30 (α = 227 μV K^{-1}, $\sigma = 9.81 \times 10^4$ S m^{-1}, κ = 1.17 W m^{-1} K^{-1}). This value is superior to that of $Bi_{0.3}Sb_{1.7}Te_{3.1}$ fabricated using Si_3N_4 balls and stainless-steel vessels [27]. Herein, suppression of contamination from the milling media resulted in the high thermoelectric performance of $Bi_{0.3}Sb_{1.7}Te_{3.01}$. The selection of the milling media affected the maximum ZT.

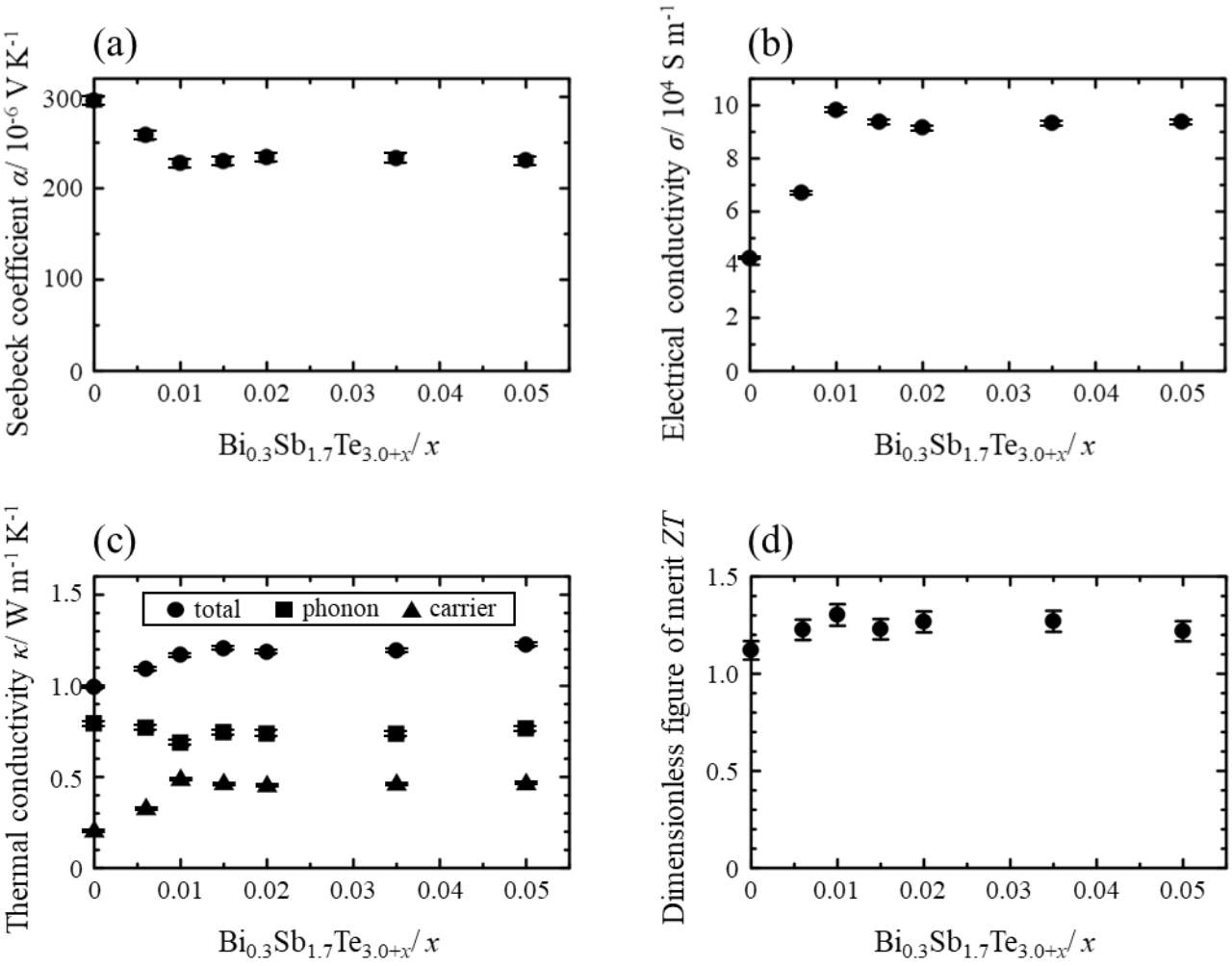

Fig. 4 Dependence of room-temperature thermoelectric properties on amount of tellurium added (x) for $Bi_{0.3}Sb_{1.7}Te_{3.0+x}$ sintered disks. (a) Seebeck coefficient, (b) electrical conductivity, (c) thermal conductivity, and (d) dimensionless figures of merit (ZT).

The temperature-dependence of the Seebeck coefficient and electrical conductivity of the sintered $Bi_{0.3}Sb_{1.7}Te_{3.01}$ disks was examined, where this sample was selected because it had the highest ZT value. The temperature-dependence of the thermoelectric properties of the undoped $Bi_{0.3}Sb_{1.7}Te_{3.0}$ sintered disk were also examined to clarify the effect of Te doping on the thermoelectric properties of $Bi_{0.3}Sb_{1.7}Te_{3.0}$. Figure 5 shows the temperature-dependence of the Seebeck coefficient for $Bi_{0.3}Sb_{1.7}Te_{3.01}$ and $Bi_{0.3}Sb_{1.7}Te_{3.0}$. All samples

showed positive α values over the entire measured temperature range, indicating that these samples had *p*-type characteristics. The Seebeck coefficient for the $Bi_{0.3}Sb_{1.7}Te_{3.0}$ bulk decreased linearly with increasing temperature. On the other hand, the Seebeck coefficient of $Bi_{0.3}Sb_{1.7}Te_{3.01}$ increased slightly with temperature up to 420 K, and subsequently decreased. These results suggest that the tellurium additive acts as a carrier dopant and suppresses excitation of the minority charge carriers (electrons) and shifts the thermal excitation temperature of the electrons toward the higher temperature range [50,51].

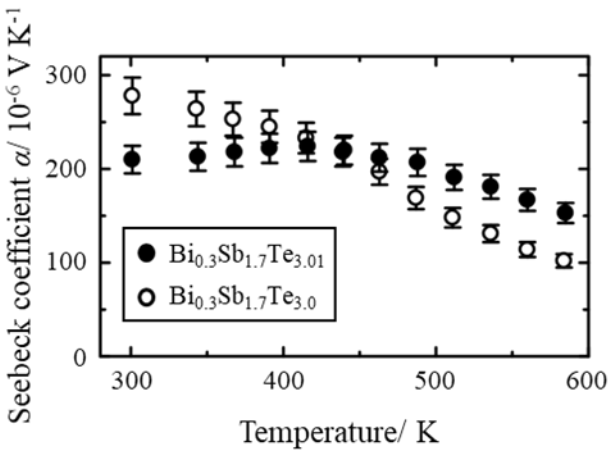

Fig. 5 Temperature-dependence of Seebeck coefficient for $Bi_{0.3}Sb_{1.7}Te_{3.01}$ and $Bi_{0.3}Sb_{1.7}Te_{3.0}$ sintered disks.

Figure 6 shows the temperature-dependence of the electrical conductivity for $Bi_{0.3}Sb_{1.7}Te_{3.01}$ and $Bi_{0.3}Sb_{1.7}Te_{3.0}$. The electrical conductivity of both samples decreased monotonically with increasing temperature, which indicates that the sintered bulk exhibited the behavior of a degenerate semiconductor. The decreasing rate in electrical conductivity for $Bi_{0.3}Sb_{1.7}Te_{3.0}$ was lower than that for $Bi_{0.3}Sb_{1.7}Te_{3.01}$. This result suggests that the intrinsic excitation occurs at a lower temperature in $Bi_{0.3}Sb_{1.7}Te_{3.0}$ bulk, which

hinders the decrease in electrical conductivity [52]. In other words, additive tellurium shifts the thermal excitation temperature toward a higher temperature range in $Bi_{0.3}Sb_{1.7}Te_{3.01}$ bulk, which is in good agreement with Seebeck coefficient measurement results.

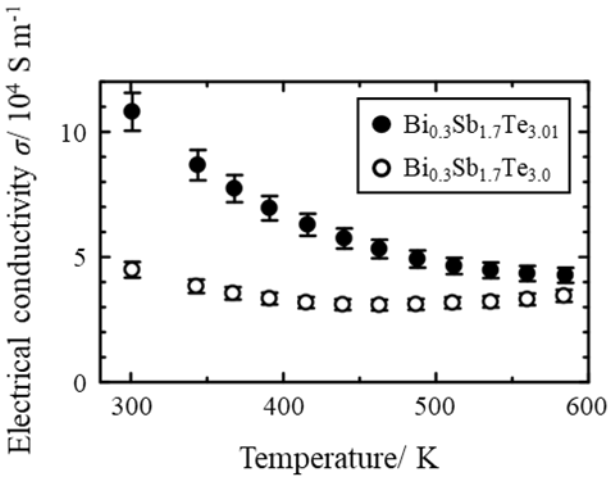

Fig. 6 Temperature-dependence of electrical conductivity for $Bi_{0.3}Sb_{1.7}Te_{3.01}$ and $Bi_{0.3}Sb_{1.7}Te_{3.0}$ sintered disks.

As a consequence, the highest *ZT* value (1.30) was obtained at room temperature with a composition of $Bi_{0.3}Sb_{1.7}Te_{3.01}$. Zhao et al. used a stainless-steel jar for ball-milling and achieved a maximum *ZT* of 1.3 at 400 K (*ZT* = 1.1 at room temperature) by dispersing nanoparticles into $Bi_{0.3}Sb_{1.7}Te_3$ [34]. However, the same value was obtained herein without nanoparticles owing to the suppression of contamination from the milling media. The high thermoelectric performance indicates that the inherent thermoelectric properties of bismuth antimony telluride were accessed by adjusting the milling media materials and Te doping, and the thermoelectric performance was improved.

4. Conclusion

The present study was carried out to investigate the thermoelectric properties of $Bi_{0.3}Sb_{1.7}Te_{3.0+x}$ (x: 0–0.05) fabricated by MA with YSZ milling media followed by HP. The results are summarized as follows.

(1) All the sintered disks were *p*-type semiconductors. All disks were dense, homogeneous, and finely grained with isotropy. The grain size of the $Bi_{0.3}Sb_{1.7}Te_{3.01}$ sintered disk was approximately 1 μm.

(2) DTA analysis of $Bi_{0.3}Sb_{1.7}Te_{3.05}$ showed tellurium precipitation and the formation of a Bi_2Te_3-Te solid-solution. The solid solubility limit of tellurium was determined to be x = 0.01. The solid-solubility of tellurium shifted within a narrow range upon changing the milling media from Si_3N_4 balls and stainless-steel vessels to YSZ balls and vessels.

(3) The dimensionless figure of merit, *ZT*, reached a maximum value of 1.30 (α = 227 μV K^{-1}, σ = 9.81 × 10^4 S m^{-1}, κ = 1.17 W m^{-1} K^{-1}) at room temperature for the $Bi_{0.3}Sb_{1.7}Te_{3.01}$ sintered bulk. The addition of tellurium required to achieve the maximum *ZT* also shifted upon changing the milling media.

The suppression of contamination from the milling media resulted in the high thermoelectric performance of bismuth antimony telluride. Thus, selection of the milling media affected the optimum doping amount and maximum *ZT*.

Acknowledgements

This study was supported by the Takahashi Industrial and Economic Research Foundation.

References

[1] G.D. Mahan, J.O. Sofo, The best thermoelectric, Proc. Natl. Acad. Sci. U. S. A. 93 (1996) 7436–7439. https://doi.org/10.1073/pnas.93.15.7436.

[2] F.J. Disalvo, Thermoelectric cooling and power generation, Science 285 (1999) 703–706. https://doi.org/10.1126/science.285.5428.703.

[3] L.E. Bell, Cooling, heating, generating power, and recovering waste heat with thermoelectric systems, Science 321 (2008) 1457–1461. https://doi.org/10.1126/science.1158899.

[4] B. Madavali, H.S. Kim, K.H. Lee, Y. Isoda, F. Gascoin, S.J. Hong, Large scale production of high efficient and robust *p*-type Bi-Sb-Te based thermoelectric materials by powder metallurgy, Mater. Des. 112 (2016) 485–494. https://doi.org/10.1016/j.matdes.2016.09.089.

[5] B. Poudel, Q. Hao, Y. Ma, Y. Lan, A. Minnich, B. Yu, X. Yan, D. Wang, A. Muto, D. Vashaee, X. Chen, J. Liu, M.S. Dresselhaus, G. Chen, Z. Ren, High-thermoelectric performance of nanostructured bismuth antimony telluride bulk alloys, Science 320 (2008) 634–638. https://doi.org/10.1126/science.1156446.

[6] H.J. Goldsmid, Bismuth telluride and its alloys as materials for thermoelectric generation, Materials 7 (2014) 2577–2592. https://doi.org/10.3390/ma7042577.

[7] Z. Chen, Z. Jian, W. Li, Y. Chang, B. Ge, R. Hanus, J. Yang, Y. Chen, M. Huang, G.J. Snyder, Y. Pei, Lattice Dislocations Enhancing Thermoelectric PbTe in Addition to Band Convergence, Adv. Mater. 29 (2017) 1606768. https://doi.org/10.1002/adma.201606768.

[8] M. Bumrungpon, I. Morioka, R. Yasufuku, T. Hirai, K. Hanasaku, K. Hirota, K. Takagi, K. Hasezaki, The critical point of average grain size in phonon thermal

conductivity of fine-grained undoped lead telluride, Mater. Trans. 61 (2020) 2025–2029. https://doi.org/10.2320/matertrans.MT-M2020069.

[9] M.H. Lee, J.H. Park, S.D. Park, J.S. Rhyee, M.W. Oh, Grain growth mechanism and thermoelectric properties of hot press and spark plasma sintered Na-doped PbTe, J. Alloys Compd. 786 (2019) 515–522. https://doi.org/10.1016/j.jallcom.2019.01.387.

[10] C. Xu, B. Duan, S. Ding, P. Zhai, Q. Zhang, Thermoelectric properties of skutterudites $Co_{4-x}Ni_xSb_{11.9-y}Te_ySe_{0.1}$, J. Electron. Mater. 43 (2014) 2224–2228. https://doi.org/10.1007/s11664-014-3016-6.

[11] G. Rogl, P. Rogl, Skutterudites, a most promising group of thermoelectric materials, Curr. Opin. Green Sustain. Chem. 4 (2017) 50–57. https://doi.org/10.1016/j.cogsc.2017.02.006.

[12] G. Rogl, A. Grytsiv, P. Heinrich, E. Bauer, P. Kumar, N. Peranio, O. Eibl, J. Horky, M. Zehetbauer, P. Rogl, New bulk *p*-type skutterudites $DD_{0.7}Fe_{2.7}Co_{1.3}Sb_{12-x}X_x$ (X = Ge, Sn) reaching $ZT > 1.3$, Acta Mater. 91 (2015) 227–238. https://doi.org/10.1016/j.actamat.2015.03.008.

[13] A. Nozariasbmarz, P. Roy, Z. Zamanipour, J.H. Dycus, M.J. Cabral, J.M. LeBeau, J.S. Krasinski, D. Vashaee, Comparison of thermoelectric properties of nanostructured Mg_2Si, $FeSi_2$, SiGe, and nanocomposites of SiGe-Mg_2Si, SiGe-$FeSi_2$, APL Mater. 4 (2016) 104814. https://doi.org/10.1063/1.4966138.

[14] Y. Gelbstein, J. Tunbridge, R. Dixon, M.J. Reece, H. Ning, R. Gilchrist, R. Summers, I. Agote, M.A. Lagos, K. Simpson, C. Rouaud, P. Feulner, S. Rivera, R. Torrecillas, M. Husband, J. Crossley, I. Robinson, Physical, mechanical, and structural properties of highly efficient nanostructured *n*- and *p*-silicides for

practical thermoelectric applications, J. Electron. Mater. 43 (2014) 1703–1711. https://doi.org/10.1007/s11664-013-2848-9.

[15] C. Gayner, K.K. Kar, Recent advances in thermoelectric materials, Prog. Mater. Sci. 83 (2016) 330–382. https://doi.org/10.1016/j.pmatsci.2016.07.002.

[16] M. Stordeur, Valence band structure and the thermoelectric figure-of-merit of $(Bi_{1-x}Sb_x)_2Te_3$ crystals, in: D.M. Rowe (Ed.), CRC Handb. Thermoelectr., CRC Press, Taylor & Francis Group, Boca Raton, Florida, 1995, p. 241.

[17] H. Scherrer, S. Scherrer, Thermoelectric properties of bismuth antimony telluride solid solutions, in: D.M. Rowe (Ed.), Thermoelectr. Handb. Macro to Nano, CRC Press, Taylor & Francis Group, Boca Raton, Florida, 2006, ch. 27.

[18] K. Hasezaki, M. Nishimura, M. Umata, H. Tsukuda, M. Araoka, Mechanical alloying of BiTe and BiSbTe thermoelectric materials, Mater. Trans. JIM. 35 (1994) 428–432. https://doi.org/10.2320/matertrans1989.35.428.

[19] M. Zakeri, M. Allahkarami, G. Kavei, A. Khanmohammadian, M.R. Rahimipour, Synthesis of nanocrystalline Bi_2Te_3 via mechanical alloying, J. Mater. Process. Technol. 209 (2009) 96–101. https://doi.org/10.1016/j.jmatprotec.2008.01.027.

[20] Y. Ma, Q. Hao, B. Poudel, Y. Lan, B. Yu, D. Wang, G. Chen, Z. Ren, Enhanced thermoelectric figure-of-merit in *p*-type nanostructured bismuth antimony tellurium alloys made from elemental chunks, Nano Lett. 8 (2008) 2580–2584. https://doi.org/10.1021/nl8009928.

[21] B.A. Cook, J.L. Harringa, Solid-state synthesis of thermoelectric materials, in: D.M. Rowe (Ed.), Thermoelectr. Handb. Macro to Nano, CRC Press, Taylor & Francis Group, Boca Raton, Florida, 2006, ch. 19.

[22] M. Kitamura, K. Hasezaki, Effect of mechanical alloying on thermal conductivity

of Bi_2Te_3-Sb_2Te_3, Mater. Trans. 57 (2016) 2153–2157. https://doi.org/10.2320/matertrans.M2016169.

[23] K. Uemura, I. Nishida, Thermoelectric semiconductor and its applications, Nikkankougyou Shinbunsha, Tokyo, 1988, pp. 145-147, 167–169, and 195–197.

[24] M. Bumrungpon, K. Hirota, K. Takagi, K. Hanasaku, T. Hirai, I. Morioka, R. Yasufuku, M. Kitamura, K. Hasezaki, Synthesis and thermoelectric properties of bismuth antimony telluride thermoelectric materials fabricated at various ball-milling speeds with yttria-stabilized zirconia ceramic vessel and balls, Ceram. Int. 46 (2020) 13869–13876. https://doi.org/10.1016/j.ceramint.2020.02.180.

[25] M.U. Muzaffar, B. Zhu, Q. Yang, Y. Zhou, S. Zhang, Z. Zhang, J. He, Suppressing bipolar effect to broadening the optimum range of thermoelectric performance for *p*-type bismuth telluride–based alloys via calcium doping, Mater. Today Phys. 9 (2019) 100130. https://doi.org/10.1016/j.mtphys.2019.100130.

[26] F. Hao, P. Qiu, Q. Song, H. Chen, P. Lu, D. Ren, X. Shi, L. Chen, Roles of Cu in the enhanced thermoelectric properties in $Bi_{0.5}Sb_{1.5}Te_3$, Materials 10 (2017) 251. https://doi.org/10.3390/ma10030251.

[27] K. Hirota, M. Kitamura, K. Takagi, K. Hasezaki, Thermoelectric behaviors of $Bi_{0.3}Sb_{1.7}Te_{3.0}$ with excess or deficiency of tellurium prepared by mechanical alloying followed by hot pressing, Mater. Trans. 59 (2018) 1233–1238. https://doi.org/10.2320/matertrans.MF201704.

[28] J. Yang, R. Chen, X. Fan, S. Bao, W. Zhu, Thermoelectric properties of silver-doped *n*-type Bi_2Te_3-based material prepared by mechanical alloying and subsequent hot pressing, J. Alloys Compd. 407 (2006) 330–333.

https://doi.org/10.1016/j.jallcom.2005.06.041.

[29] B. Madavali, H. Kim, S.J. Hong, Reduction of thermal conductivity in Al_2O_3 dispersed *p*-type bismuth antimony telluride composites, Mater. Chem. Phys. 233 (2019) 9–15. https://doi.org/10.1016/j.matchemphys.2019.05.023.

[30] S. Wang, H. Li, R. Lu, G. Zheng, X. Tang, Metal nanoparticle decorated *n*-type Bi_2Te_3-based materials with enhanced thermoelectric performances, Nanotechnology 24 (2013) 285702. https://doi.org/10.1088/0957-4484/24/28/285702.

[31] M.Y. Kim, Y.H. Yeo, D.H. Park, T.S. Oh, Thermoelectric characteristics of the $(Bi,Sb)_2(Te,Se)_3$ nanocomposites processed with nanoparticle dispersion, Ceram. Int. 38 (2012) S529–S533. https://doi.org/10.1016/j.ceramint.2011.05.069.

[32] M. Deng, Y. Huang, Dispersing $Bi_2Mo_2O_9$ nanoparticles into $Bi_{0.5}Sb_{1.5}Te_3$ alloys for enhanced thermoelectric figure of merit (*ZT*) through phonon scattering, Ceram. Int. 45 (2019) 24914–24918. https://doi.org/10.1016/j.ceramint.2019.08.150.

[33] K. Ahmad, C. Wan, P. an Zong, Thermoelectric properties of BiSbTe/graphene nanocomposites, J. Mater. Sci. Mater. Electron. 30 (2019) 11923–11930. https://doi.org/10.1007/s10854-019-01538-z.

[34] L. Zhao, W. Qiu, Y. Sun, L. Chen, H. Deng, L. Yang, X. Shi, J. Tang, Enhanced thermoelectric performance of $Bi_{0.3}Sb_{1.7}Te_3$ based alloys by dispersing TiC ceramic nanoparticles, J. Alloys Compd. 863 (2021) 158376. https://doi.org/10.1016/j.jallcom.2020.158376.

[35] Y. Pan, Y. Qiu, I. Witting, L. Zhang, C. Fu, J.W. Li, Y. Huang, F.H. Sun, J. He, G.J. Snyder, C. Felser, J.F. Li, Synergistic modulation of mobility and thermal

conductivity in $(Bi,Sb)_2Te_3$ towards high thermoelectric performance, Energy Environ. Sci. 12 (2019) 624–630. https://doi.org/10.1039/c8ee03225d.

[36] A.A. Abdelnabi, V. Lakhian, J.R. McDermid, Y.C. Tseng, J.S. Cotton, Enhancement of mechanical properties and thermoelectric performance of spark plasma sintered *p*-type bismuth telluride by powder surface oxide reduction, J. Alloys Compd. 858 (2021) 157657. https://doi.org/10.1016/j.jallcom.2020.157657.

[37] S.S. Lim, B.K. Kim, S.K. Kim, H.H. Park, D.I. Kim, D. Bin Hyun, J.S. Kim, S.H. Baek, A two-step synthesis process of thermoelectric alloys for the separate control of carrier density and mobility, J. Alloys Compd. 727 (2017) 191–195. https://doi.org/10.1016/j.jallcom.2017.08.089.

[38] S. Cho, Y. Kim, A. DiVenere, G.K. Wong, J.B. Ketterson, J.R. Meyer, Antisite defects of Bi_2Te_3 thin films, Appl. Phys. Lett. 75 (1999) 1401–1403. https://doi.org/10.1063/1.124707.

[39] P.P. Murmu, J. Kennedy, S. Suman, S. V. Chong, J. Leveneur, J. Storey, S. Rubanov, G. Ramanath, Multifold improvement of thermoelectric power factor by tuning bismuth and antimony in nanostructured *n*-type bismuth antimony telluride thin films, Mater. Des. 163 (2019) 107549. https://doi.org/10.1016/j.matdes.2018.107549.

[40] T.J. Zhu, L.P. Hu, X.B. Zhao, J. He, New insights into intrinsic point defects in V_2VI_3 thermoelectric materials, Adv. Sci. 3 (2016) 1600004. https://doi.org/10.1002/advs.201600004.

[41] S. Turenne, T. Clin, D. Vasilevskiy, R.A. Masut, Finite element thermomechanical modeling of large area thermoelectric generators based on

bismuth telluride alloys, J. Electron. Mater. 39 (2010) 1926–1933. https://doi.org/10.1007/s11664-009-1049-z.

[42] C. Chen, B. Zhang, D. Liu, Z. Ge, Thermoelectric properties of $Cu_yBi_xSb_{2-x-y}Te_3$ alloys fabricated by mechanical alloying and spark plasma sintering, Intermetallics 25 (2012) 131–135. https://doi.org/10.1016/j.intermet.2012.02.018.

[43] K. Hirota, K. Takagi, K. Hanasaku, K.L. Hasezaki, H. Saito, S. Hata, K. Hasezaki, Carbon observation by electron energy-loss spectroscopy and thermoelectric properties of graphite added bismuth antimony telluride prepared by mechanical alloying-hot pressing, Intermetallics 109 (2019) 1–7. https://doi.org/10.1016/j.intermet.2019.03.005.

[44] M. Fusa, N. Yamamoto, K. Hasezaki, Measurement of Seebeck coefficient and conductive behaviors of $Bi_2Te_{3-x}Se_x$ (x = 0.15-0.6) thermoelectric semiconductors without harmful dopants, Mater. Trans. 55 (2014) 942–946. https://doi.org/10.2320/matertrans.MB201301.

[45] N.D. Lowhorn, W. Wong-Ng, Z.Q. Lu, E. Thomas, M. Otani, M. Green, N. Dilley, J. Sharp, T.N. Tran, Development of a Seebeck coefficient standard reference material, Appl. Phys. A Mater. Sci. Process. 96 (2009) 511–514. https://doi.org/10.1007/s00339-009-5191-5.

[46] T.M. Tritt, Thermal conductivity: theory, properties, and applications, Kluwer Academic/Plenum Publishers, New York, 2004, pp.193–195.

[47] K. Hasezaki, S. Wakazuki, T. Fujii, M. Kitamura, Constituent element addition to *n*-type $Bi_2Te_{2.67}Se_{0.33}$ thermoelectric semiconductor without harmful dopants by mechanical alloying, Mater. Trans. 57 (2016) 1001–1005. https://doi.org/10.2320/matertrans.M2016031.

[48] S.D. Kang, G.J. Snyder, Transport property analysis method for thermoelectric materials: material quality factor and the effective mass model, arXiv preprint arXiv:1710.06896, (2017) 1–5.

[49] S.A. Humphry-Baker, C.A. Schuh, Spontaneous solid-state foaming of nanocrystalline thermoelectric compounds at elevated temperatures, Nano Energy 36 (2017) 223–232. https://doi.org/10.1016/j.nanoen.2017.04.018.

[50] Z. Xu, H. Wu, T. Zhu, C. Fu, X. Liu, L. Hu, J. He, J. He, X. Zhao, Attaining high mid-temperature performance in $(Bi,Sb)_2Te_3$ thermoelectric materials via synergistic optimization, NPG Asia Mater. 8 (2016) e302. https://doi.org/10.1038/am.2016.134.

[51] L.P. Hu, T.J. Zhu, Y.G. Wang, H.H. Xie, Z.J. Xu, X.B. Zhao, Shifting up the optimum figure of merit of *p*-type bismuth telluride-based thermoelectric materials for power generation by suppressing intrinsic conduction, NPG Asia Mater. 6 (2014) e88. https://doi.org/10.1038/am.2013.86.

[52] Z. Wei, C. Wang, J. Zhang, J. Yang, Z. Li, Q. Zhang, P. Luo, W. Zhang, E. Liu, J. Luo, Precise regulation of carrier concentration in thermoelectric BiSbTe alloys via magnetic doping, ACS Appl. Mater. Interfaces. 12 (2020) 20653–20663. https://doi.org/10.1021/acsami.0c02408.